nature materials

Article

https://doi.org/10.1038/s41563-023-01774-z

Field-free switching of perpendicular magnetization by two-dimensional $PtTe_2/WTe_2$ van der Waals heterostructures with high spin Hall conductivity

Received: 8 July 2022

Accepted: 28 November 2023

Published online: 19 January 2024

Check for updates

Fei Wang[1,8], Guoyi Shi[1,2,8], Kyoung-Whan Kim[3,8], Hyeon-Jong Park[4], Jae Gwang Jang[5], Hui Ru Tan[6], Ming Lin[6], Yakun Liu[1], Taeheon Kim[1], Dongsheng Yang[1], Shishun Zhao[1], Kyusup Lee[1], Shuhan Yang[1], Anjan Soumyanarayanan[6,7], Kyung-Jin Lee[5] ✉ & Hyunsoo Yang[1,2] ✉

The key challenge of spin–orbit torque applications lies in exploring an excellent spin source capable of generating out-of-plane spins while exhibiting high spin Hall conductivity. Here we combine $PtTe_2$ for high spin conductivity and WTe_2 for low crystal symmetry to satisfy the above requirements. The $PtTe_2/WTe_2$ bilayers exhibit a high in-plane spin Hall conductivity $\sigma_{s,y} \approx 2.32 \times 10^5 \times \hbar/2e\ \Omega^{-1}\,m^{-1}$ and out-of-plane spin Hall conductivity $\sigma_{s,z} \approx 0.25 \times 10^5 \times \hbar/2e\ \Omega^{-1}\,m^{-1}$, where $\hbar$ is the reduced Planck's constant and e is the value of the elementary charge. The out-of-plane spins in $PtTe_2/WTe_2$ bilayers enable the deterministic switching of perpendicular magnetization at room temperature without magnetic fields, and the power consumption is 67 times smaller than that of the Pt control case. The high out-of-plane spin Hall conductivity is attributed to the conversion from in-plane spin to out-of-plane spin, induced by the crystal asymmetry of WTe_2. Our work establishes a low-power perpendicular magnetization manipulation based on wafer-scale two-dimensional van der Waals heterostructures.

According to the conventional spin Hall physics in a heavy-metal/ferromagnet (HM/FM) system, an in-plane charge current (J_e) flowing along the x direction in the HM layer gives rise to a spin current, flowing to the z direction with the spin polarization along the y direction (Fig. 1a)[1–3]. The y-polarized spin current facilitates the magnetization switching of the adjacent FM with in-plane magnetic anisotropy; however, its application for the switching of a perpendicularly magnetized FM is non-deterministic[1,4]. To manipulate a FM with perpendicular magnetic anisotropy for high-density data storage applications, an external assisting magnetic field (H) along the current direction is required (Fig. 1a). The spin current with out-of-plane spins (z spins) can overcome the limitation of external magnetic fields[5]. The z spins are often created in low-crystal-symmetry materials with at most one mirror plane and no n-fold ($n > 1$) rotational invariance[6], for example, $MoTe_2$ (refs. 7,8),

[1]Department of Electrical and Computer Engineering, National University of Singapore, Singapore, Singapore. [2]Integrative Sciences and Engineering Programme, NUS Graduate School, National University of Singapore, Singapore, Singapore. [3]Center of Spintronics, Korea Institute of Science and Technology, Seoul, Korea. [4]KU-KIST Graduate School of Converging Science and Technology, Korea University, Seoul, Korea. [5]Department of Physics, Korea Advanced Institute of Science and Technology (KAIST), Daejeon, Korea. [6]Institute of Materials Research & Engineering, Agency for Science Technology & Research (A*STAR), Singapore, Singapore. [7]Department of Physics, National University of Singapore, Singapore, Singapore. [8]These authors contributed equally: Fei Wang, Guoyi Shi, Kyoung-Whan Kim. ✉e-mail: kjlee@kaist.ac.kr; eleyang@nus.edu.sg

https://doi.org/10.1038/s41563-023-01774-z

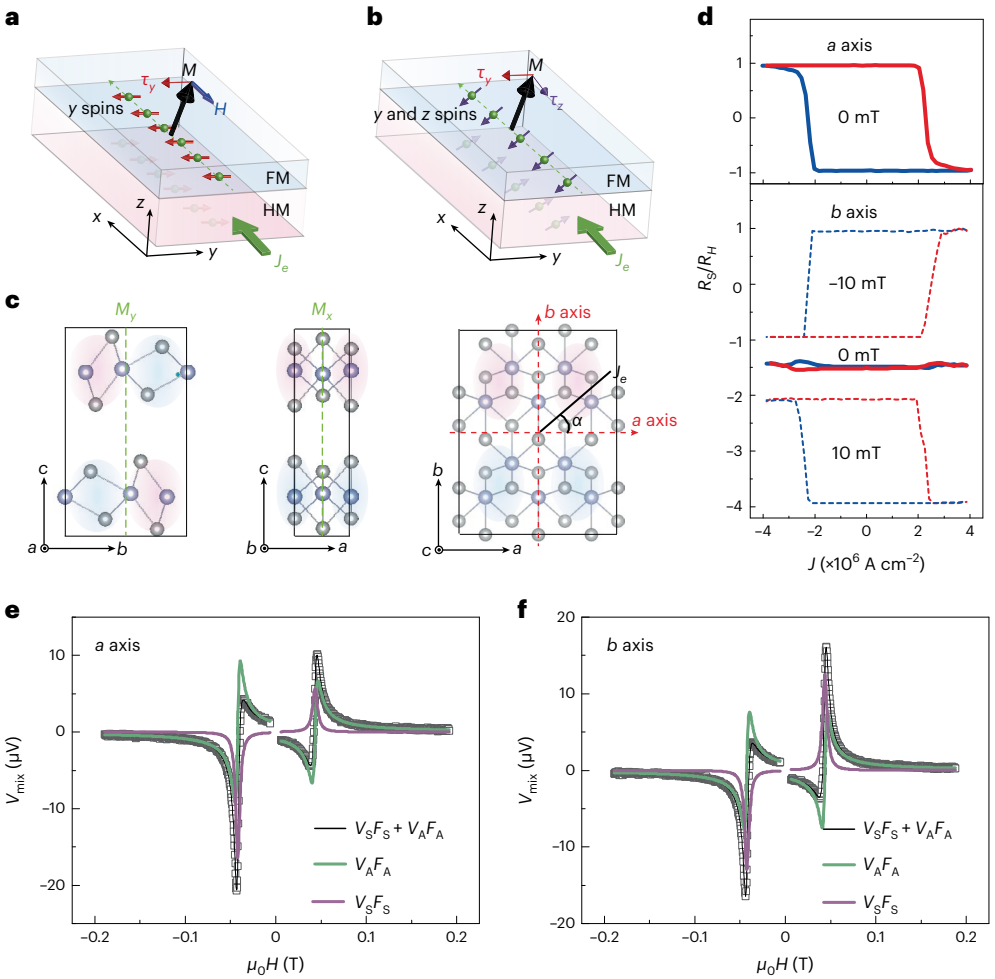

Fig. 1 | Crystal symmetry and SOT of the WTe_2 layer. a, Schematic of a SOT device in a HM/FM with perpendicular magnetic anisotropy. An in-plane charge current J_e generates out-of-plane spin currents with *y*-polarized spins. The *y*-polarized spins exert an in-plane anti-damping torque $\mathbf{m} \times \mathbf{y} \times \mathbf{m}$ (τ_y) on the magnetization (M) in the FM layer. In this case, an external magnetic field along the current direction is required for deterministic switching of the FM. **b**, Schematic of a SOT device in a HM/FM bilayer, where the HM can create *z*-polarized spins. The in-plane charge current generates both *y*- and *z*-polarized spins. The *z*-polarized spins exert an out-of-plane anti-damping torque $\mathbf{m} \times \mathbf{z} \times \mathbf{m}$ (τ_z), which enables deterministic switching of the FM without any external magnetic field. **c**, Crystal structure of WTe_2 ($Pmn2_1$) and the two mirror symmetries. One is pure mirror M_x and the other is a glide mirror M_y. The *a*, *b* and *c* arrows represent the crystal axes. **d**, Deterministic current-induced magnetization switching with currents along the *a* axis (top panel) and *b* axis (bottom panel) in the WTe_2 (8 nm)/CoFeB sample. *J* is the current density. **e**,**f**, ST-FMR data from WTe_2 (8 nm)/Py at 5 GHz with currents applied along the *a* axis (**e**) of the WTe_2 layer and the *b* axis (**f**). The solid lines are fits with symmetric (V_SF_S; purple) and anti-symmetric (V_AF_A; green) Lorentzians. μ_0 is the vacuum permeability.

CuPt (ref. 9), $TaTe_2$ (ref. 10) and WTe_2 (refs. 11–16). In these systems, both *y*- and *z*-polarized spins flow along the *z* direction and switch the perpendicularly magnetized FM at zero magnetic field (Fig. 1b). However, the highest reported in-plane spin Hall conductivity in these materials is only $8 \times 10^3 \times \hbar/2e\ \Omega^{-1}\,m^{-1}$ (Supplementary Table 1), which is much smaller than those from topological insulators[17,18] and conventional HM[19,20] such as Pt and Ta at room temperature ($\sim 10^5 \times \hbar/2e\ \Omega^{-1}\,m^{-1}$). This causes significant current shunting as well as huge power-consumption issues. Therefore, a suitable spin source material should be able not only to generate *z* spins strong enough to deterministically switch a FM with perpendicular magnetic anisotropy, but also to possess a high spin Hall conductivity ($\sigma_{s,y} > 10^5 \times \hbar/2e\ \Omega^{-1}\,m^{-1}$) to minimize the power consumption. A single material system has so far been unable to simultaneously meet the above two requirements.

The integration of two-dimensional van der Waals materials into heterostructures not only amalgamates the functionalities of component materials, but also engenders novel electronic phases, thereby allowing for the design of artificial structures with predetermined attributes[21–24]. Such an approach is particularly compelling for spin–orbit torque (SOT) technologies. In this work, we combine WTe_2 with low crystal symmetry and $PtTe_2$ with high spin Hall conductivity in the form of van der Waals heterostructures. As compared to the WTe_2 alone, the $PtTe_2/WTe_2$ bilayers exhibit a 17 times larger in-plane spin Hall conductivity, eight times larger out-of-plane spin Hall conductivity and associated field-free SOT switching of perpendicular magnetization with 33 times lower power. The larger out-of-plane spin accumulation in the $PtTe_2/WTe_2$ bilayers is attributed to the spin-to-spin conversion in the symmetry-broken WTe_2 layer.

We first prepare a single layer of WTe_2 and evaluate the SOT in WTe_2/FM. In WTe_2, the glide symmetry is broken along the low-symmetry *a* axis, but the mirror symmetry along the *b* axis is preserved, as illustrated in Fig. 1c. In this case, both the *y* and *z* spins are generated for the current injected along the *a* axis of WTe_2. We grow WTe_2 films with different thicknesses (t = 1.5, 3, 4.5, 6 and 8 nm) on sapphire (001) substrates using molecular beam epitaxy (MBE; Methods for details). The high crystalline quality and smooth surface of WTe_2 films are confirmed

https://doi.org/10.1038/s41563-023-01774-z

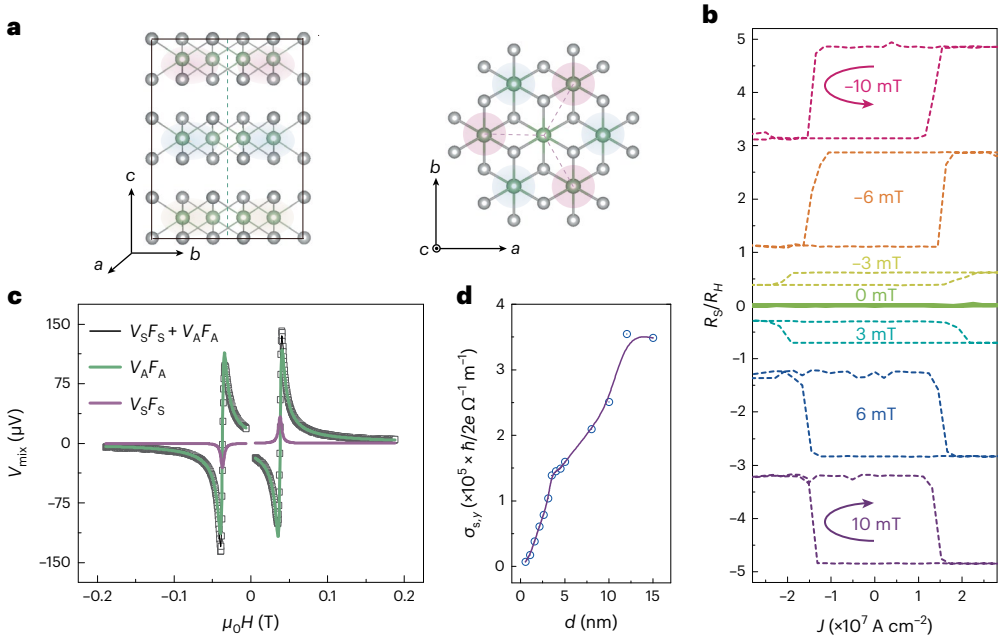

Fig. 2 | Crystal symmetry and SOT in $PtTe_2$. **a**, Crystal structure of $PtTe_2$ ($P\bar{3}m1$). $PtTe_2$ shows an in-plane three-fold symmetry. **b**, Deterministic current-induced magnetization switching under different in-plane fields in the $PtTe_2$ (8 nm)/CoFeB heterostructure. The arrows indicate the switching directions. The data are shifted vertically for clarity. **c**, ST-FMR spectra from the $PtTe_2$ (8 nm)/Py sample at 5 GHz. The solid lines are fits that show the symmetry (V_SF_S; purple) and anti-symmetry (V_AF_A; green) Lorentzian contributions. **d**, $PtTe_2$ thickness-dependent in-plane spin Hall conductivity $\sigma_{s,y}$, where d is thickness.

by reflection high-energy electron diffraction, atomic force microscopy and X-ray diffraction (Supplementary Note 1). The crystal axes of the WTe_2 films can be distinguished by the polarized Raman, terahertz and transport measurements (Supplementary Notes 2–4). The subsequent growth is carried out in a magnetron sputtering chamber to form WTe_2 (t)/Ti (2)/$Co_{0.2}Fe_{0.6}B_{0.2}$ (0.9)/MgO (2)/Ta (1.5) heterostructures (henceforth written as WTe_2 (t)/CoFeB, where the thickness is in parentheses, in nanometres), where Ta is oxidized upon exposure to air. Then WTe_2/CoFeB heterostructures are fabricated into Hall bar devices by varying the angle (α) between the a axis of WTe_2 and current injection direction, as depicted in the right panel of Fig. 1c. The CoFeB layer exhibits perpendicular magnetic anisotropy for all devices. We then apply a pulsed d.c. current and measure the Hall resistance at room temperature. The current-induced magnetization switching of the WTe_2 (8 nm)/CoFeB sample with the current applied along the a axis is shown in the top panel of Fig. 1d. We observe a full magnetization switching ($R_S/R_H \approx 1$, where R_S and R_H are the Hall resistance changes in response to the SOT and magnetic field, respectively) at zero magnetic field, which indicates the generation of z spins. However, when the current is applied along the b axis, an in-plane magnetic field along the current direction is required for a deterministic switching of the FM due to the absence of z spins, as shown in the bottom panel of Fig. 1d.

The y- and z-polarized spin currents generated from the WTe_2 spin source layer can be quantified by the spin-torque ferromagnetic resonance (ST-FMR) technique[19,25] (Supplementary Note 5). The ST-FMR devices of WTe_2 (t)/$Ni_{81}Fe_{19}$ (6)/SiO_2 (2)/Ta (1.5) (abbreviated WTe_2 (t)/Py), where the Py layer exhibits an in-plane magnetic anisotropy, are fabricated with different α values relative to the a axis of the WTe_2 layer. Figure 1e shows representative ST-FMR signals V_{mix} for the WTe_2 (8 nm)/Py sample with the current applied along the a axis. We note that V_{mix} is quite different in both shape and amplitude for the positive and negative external magnetic fields, which can be ascribed to additional z-spin-induced damping-like ($\mathbf{m} \times \mathbf{z} \times \mathbf{m}$) and field-like ($\mathbf{m} \times \mathbf{z}$) torques, where $\mathbf{m}$ and $\mathbf{z}$ are the unit vector along the magnetization and the z direction, respectively[26]. As a comparison, we also measure when the current is injected along the b axis, shown in Fig. 1f. The magnitude of V_{mix} is the same for the positive and negative external magnetic fields, indicating that torques are limited to y-spin-induced damping-like ($\mathbf{m} \times \mathbf{y} \times \mathbf{m}$) and field-like ($\mathbf{m} \times \mathbf{y}$) torques, where $\mathbf{y}$ is the unit vector along the y direction.

Following the established analysis method[19], we extract the in-plane and out-of-plane effective spin-torque efficiencies to be $\theta_y = 0.15$ and $\theta_z = -0.034$, respectively. The negative θ_z indicates the generation of up (down) spins for a positive (negative) current in our experimental geometry, which is consistent with the current-induced magnetization switching and loop shift measurements (Supplementary Note 6). The room temperature resistivity ρ_{xx} of the 8 nm WTe_2 film is 1,123 μΩ cm and thus the in-plane and out-of-plane spin Hall conductivities are determined to be $\sigma_{s,y} = 1.335 \times 10^4 \times \hbar/2e\ \Omega^{-1}\,m^{-1}$ and $\sigma_{s,z} = -0.3 \times 10^4 \times \hbar/2e\ \Omega^{-1}\,m^{-1}$, respectively. Due to the highly resistive nature of semiconducting WTe_2 (Supplementary Figs. 7 and 8), $\sigma_{s,y}$ is an order of magnitude smaller than those of other spin source materials[17–20]. Therefore, enhancing the spin Hall conductivity of WTe_2 while maintaining enough z spins is highly desirable.

The full space group notation of $PtTe_2$ is $P\bar{3}m1$, which has a hexagonal crystal structure. As shown in Fig. 2a, there is a three-fold rotation axis about the c axis; such symmetries forbid the presence of z spins in $PtTe_2$ (ref. 6). We grow the $PtTe_2$ layer with different thicknesses (d) by MBE on sapphire substrates to be followed by a FM layer using magnetron sputtering to form $PtTe_2$ (d)/FM heterostructures (Methods). Figure 2b shows the current-induced switching in the $PtTe_2$ (8 nm)/CoFeB device. The switching loop disappears at zero magnetic field, indicating the absence of z spins in the $PtTe_2$ layer. The switching behaviour is similar to that of a conventional HM/FM heterostructure in which an in-plane external magnetic field is required for deterministic switching of the FM with perpendicular magnetic anisotropy[1,4]. Upon reversing the direction of the external magnetic field, the polarity of the switching loops is reversed as well, which is consistent with the conventional SOT switching behaviour[1,4]. We also carry out ST-FMR measurements in $PtTe_2$ (d)/Py devices. The representative ST-FMR spectrum of a $PtTe_2$ (8 nm)/Py device is shown in Fig. 2c. In contrast to Fig. 1e, V_{mix} shows a nearly identical line shape and magnitude for the

https://doi.org/10.1038/s41563-023-01774-z

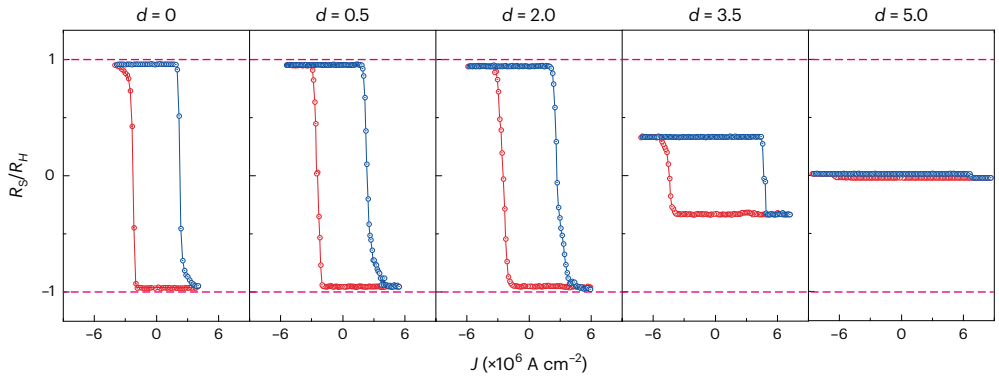

Fig. 3 | Deterministic current-induced magnetization switching in $PtTe_2$ (d)/WTe_2 (8 − d)/CoFeB heterostructures. The d = 0, 0.5, 2.0, 3.5 and 5.0 nm at zero magnetic field. Red (blue) lines and dots represent the switching sequence for decreasing (increasing) the current density. The dashed purple lines correspond to +1 or −1 of R_S/R_H.

positive and negative magnetic fields, confirming the absence of z spins in the $PtTe_2$ layer. This is consistent with the two-fold rotational symmetry in $PtTe_2$/Py samples, where the torques change the sign by reversing the external magnetic field. We extract the in-plane spin Hall conductivity $\sigma_{s,y}$ as a function of d in Fig. 2d. The $\sigma_{s,y}$ increases in a thicker $PtTe_2$ layer and saturates for $d \geq 12$ nm with $\sigma_{s,y} \approx 3.5 \times 10^5 \times \hbar/2e\ \Omega^{-1}\,m^{-1}$, comparable to the value of previous reports[27]. Moreover, at a fixed thickness of d = 8.0 nm, $\sigma_{s,y} \approx 2.1 \times 10^5 \times \hbar/2e\ \Omega^{-1}\,m^{-1}$ is 16 times larger than that of WTe_2, indicating a high $\sigma_{s,y}$ of the $PtTe_2$ layer.

As confirmed above, WTe_2 exhibits z spins but with a small spin Hall conductivity. $PtTe_2$ shows a large spin Hall conductivity without z spins. In order to synthesize a spin source material with both high spin Hall conductivity and z spins, we combine WTe_2 and $PtTe_2$ in the form of bilayer heterostructures. The sharp interface of the $PtTe_2$/WTe_2 bilayer is confirmed by transmission electron microscopy (Supplementary Note 1). For ease of comparison, we fix the total thickness of $PtTe_2$/WTe_2 heterostructures at 8 nm, while changing the thickness of individual $PtTe_2$ and WTe_2 layers. Figure 3 shows the current-induced switching of $PtTe_2$ (d)/WTe_2 (8 − d)/CoFeB samples with the current along the a axis of WTe_2 without any magnetic field. For d = 0, 0.5 and 2.0 nm, a complete field-free switching is observed (that is $R_S/R_H \approx 1$). The critical switching current density (J_c) of WTe_2 (d = 0) is 2.25×10^6 A cm^{-2}, which is one order smaller than that of the conventional HM Pt source ($J_c \approx 2.6 \times 10^7$ A cm^{-2}; Supplementary Note 7). With d increasing from 0 to 2 nm, J_c increases slightly to 2.6×10^6 A cm^{-2}. With further increasing d, R_S/R_H decreases, and the switching loop vanishes for $d \geq 5$ nm.

Figure 4a summarizes the d dependence of θ_y and θ_z obtained from ST-FMR measurements of the $PtTe_2$ (d)/WTe_2 (8 − d)/Py samples. The magnitude of both θ_y and θ_z decreases with increasing d, in agreement with the trend of the J_c and R_S/R_H from the current-induced magnetization switching measurements in Fig. 3. The out-of-plane spin canting angle β, defined as $\beta = \arctan(\theta_z/\theta_y)$, is calculated to be −12.8° for d = 0 nm, −12.1° for d = 0.5 nm and −3.5° for d = 2.0 nm, which indicates that y spins become more dominant with a thicker $PtTe_2$ layer.

We further extract $\sigma_{s,y}$ and $\sigma_{s,z}$ of $PtTe_2$ (d)/WTe_2 (8 − d) as shown in Fig. 4b. The $\sigma_{s,y}$ first increases with increasing d, and then saturates at $\sigma_{s,y} \approx 2.32 \times 10^5 \times \hbar/2e\ \Omega^{-1}\,m^{-1}$ for $d > 2$ nm. Moreover, a significant magnitude of $\sigma_{s,z} \approx 0.17$–$0.25 \times 10^5 \times \hbar/2e\ \Omega^{-1}\,m^{-1}$ is observed only when the thickness of WTe_2 is greater than 4.5 nm. We also compare the power consumption based on a two-current model[28] (Supplementary Note 8) in Fig. 4c. With the introduction of $PtTe_2$, the power consumption significantly decreases and reaches a minimum at d = 2.0 nm. The power consumption of the sample of d = 2.0 nm is 33 times smaller than its parent material WTe_2 and 67 times smaller than that of the Pt-based control sample (Supplementary Table 2).

An important experimental observation is that the $\sigma_{s,z}$ of the $PtTe_2$/WTe_2 bilayer is an order of magnitude larger than that of the WTe_2 single layer. This value contrasts with the $\sigma_{s,y}$ value of the bilayer, which is only slightly larger than that of the $PtTe_2$ single layer. This large increase of $\sigma_{s,z}$ for the bilayer cannot be described by a simple weighted average of the $\sigma_{s,z}$ of the $PtTe_2$ single layer and that of the WTe_2 single layer. Therefore, it requires an additional conversion process beyond the established charge-to-spin conversion or spin swapping effect[29–32] (Supplementary Note 9). In the bilayer, owing to the low resistance of $PtTe_2$, a significant portion of the current, over 68%, is channelled through the $PtTe_2$ layer (Supplementary Table 3). It generates y spins that are subsequently injected into the WTe_2 layer. If the WTe_2 layer can convert these y spins to z spins, it may explain the large increase in the $\sigma_{s,z}$ of the $PtTe_2$/WTe_2 bilayer. As shown below, our theory describes how such spin-to-spin conversion, realized by the crystal asymmetry of WTe_2, accounts for our experimental results.

First, we examine general symmetry properties of the spin-to-spin conversion, which is described as a linear response of spin density to an externally injected spin current, that is, $\delta S_i = \eta^k_{ij} Q^k_{s,j}$ where δS_i is the generated spin density with spin i; $Q^k_{s,j}$ is an input spin current flowing along the j direction with spin k; and η^k_{ij} is the tensor consisting of 27 components (for i, j, $k = x$, y, z) that relate $Q^k_{s,j}$ and S_i. For an inversion-symmetric crystal, all 27 components of η^k_{ij} should be zero since $Q^k_{s,j} \rightarrow -Q^k_{s,j}$ under the inversion operation, while $\delta S_i \rightarrow \delta S_i$. However, the crystal symmetry breaking allows some of the η^k_{ij} values to be non-zero. We characterize the symmetry breakings required for non-zero η^k_{ij} values of all 27 components (Supplementary Table 4). In WTe_2, the inversion symmetry and the mirror symmetry with respect to the z–x plane are broken. According to Supplementary Table 4, seven coefficients (η^y_{ii}, η^i_{iy}, η^i_{yi} for $i = x, y, z$) are allowed to be non-zero in WTe_2. Focusing on spin currents flowing along the z direction, which is relevant to the SOT, two coefficients η^y_{zz} and η^z_{yz} turn out to be non-zero. The former, η^y_{zz}, corresponds to the spin-to-spin conversion in our experiment; a y-polarized spin current $Q^y_{s,z}$, generated in $PtTe_2$, is converted to z spin S_z in WTe_2. The latter, η^z_{yz}, corresponds to the inverse process. Our symmetry argument shows that, therefore, the desired spin-to-spin conversion process describing our experiment is allowed in WTe_2.

To illustrate the spin-to-spin conversion within linear response theory, we solve the quantum Liouville equation (Supplementary Note 10) for a model Hamiltonian $\mathcal{H}(\mathbf{k})$ with a Rashba-like spin–orbit coupling that describes the mirror symmetry breaking with respect to the z–x plane as in WTe_2: $\mathcal{H}(\mathbf{k}) = \epsilon(\mathbf{k}) + \alpha_R \boldsymbol{\sigma} \cdot (\mathbf{k} \times \mathbf{y})$ where $\varepsilon(\mathbf{k})$ is a mirror symmetric dispersion, α_R is the Rashba parameter and $\mathbf{k}$ is the

https://doi.org/10.1038/s41563-023-01774-z

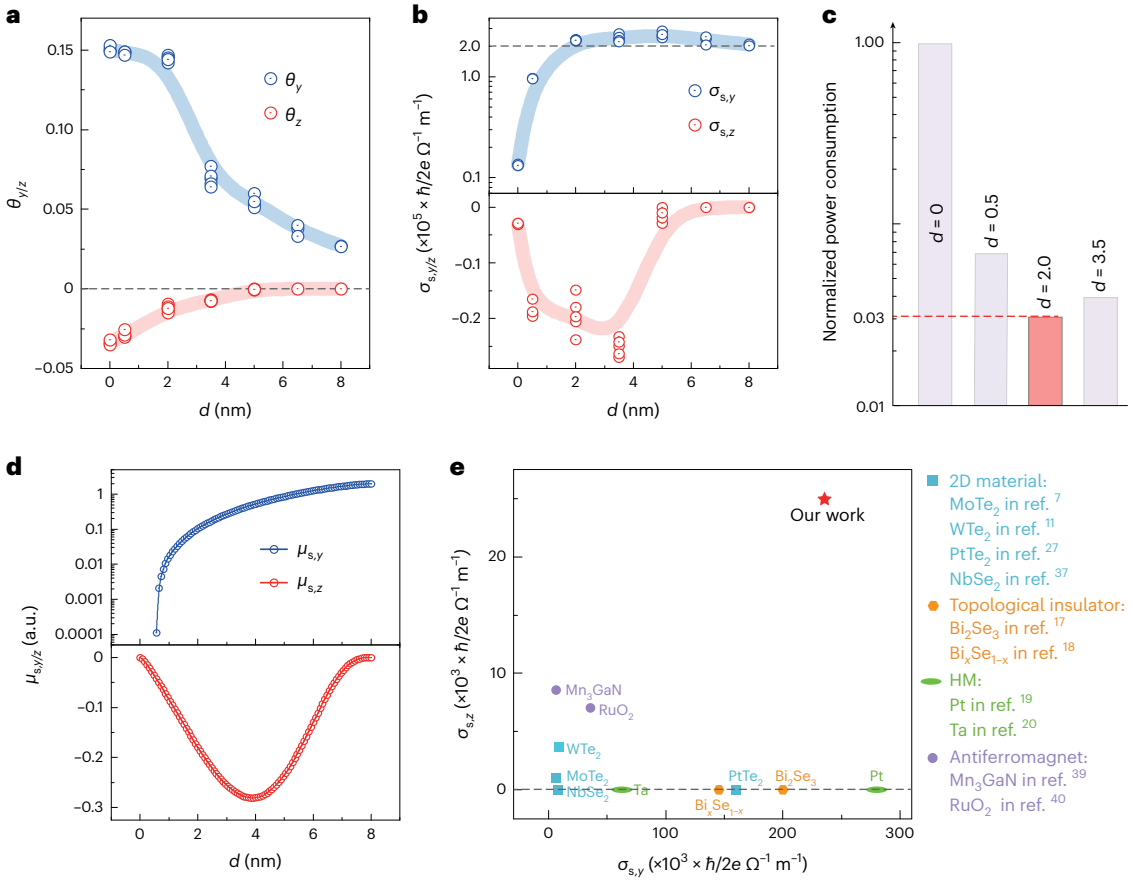

Fig. 4 | Spin Hall conductivity of $PtTe_2/WTe_2$ bilayers. a, The d dependence of in-plane and out-of-plane effective spin-torque efficiencies (θ_y and θ_z) in $PtTe_2$ (d)/WTe_2 (8 − d)/Py heterostructures. The effective spin-torque efficiencies are obtained from ST-FMR measurements. **b**, The d dependence of $\sigma_{s,y}$ and out-of-plane spin Hall conductivity $\sigma_{s,z}$ in $PtTe_2$ (d)/WTe_2 (8 − d)/Py heterostructures. The shaded areas in **a** and **b** are guidelines and the dashed black line in **b** corresponds to 2.0 of $\sigma_{s,y}$. **c**, Comparison of the normalized power consumption based on $PtTe_2$ (d)/WTe_2 (8 − d)/CoFeB heterostructures (d = 0, 0.5, 2.0 and 3.5 nm). The dashed red line corresponds to 0.03 of normalized power consumption. **d**, The d dependence of spin chemical potential $\mu_{s,y}$ for the y spin and $\mu_{s,z}$ for the z spin in $PtTe_2$ (d)/WTe_2 (8 − d) heterostructures calculated from the drift-diffusion formalism. Here we use 4.3 nm and 5.1 nm for the spin diffusion lengths of WTe_2 and $PtTe_2$, respectively (Supplementary Figs. 16a and 18); inverse of the spin-to-spin conversion length $\kappa = 0.33\ nm^{-1}$; and the electrical conductivity ratio between WTe_2 and $PtTe_2$ $\sigma_{WTe_2}/\sigma_{PtTe_2} = 0.01$. **e**, Comparison of the in-plane and out-of-plane spin Hall conductivity values with those of other spin source materials; 2D, two-dimensional.

crystal momentum of electrons, which differs from the conventional Rashba Hamiltonian. The non-equilibrium spin density obtained from the quantum Liouville equation up to the first order in α_R becomes (Supplementary Note 10)

$$\delta\mathbf{S} = \sum_{\mathbf{k}} \left[\delta\mathbf{S}^0_{\mathbf{k}} + 2\alpha_R \tau (\mathbf{k} \times \mathbf{y}) \times \delta\mathbf{S}^0_{\mathbf{k}}\right] \quad (1)$$

where $\delta\mathbf{S}$ is the non-equilibrium spin density that is injected externally, and $\delta\mathbf{S}^0_{\mathbf{k}}$ refers to its $\mathbf{k}$-resolved contribution. τ is the relaxation time. In our experiment, an externally injected y spin flows along the z direction (that is, the spin Hall current generated from $PtTe_2$) so that $\delta\mathbf{S}^0_{\mathbf{k}} \propto k_z\mathbf{y}$. Then the second term in equation (1) gives an additional spin density proportional to $\sum_{\mathbf{k}} 2\alpha_R \tau k_z^2 \mathbf{z}$, which is the z-spin accumulation owing to the spin-to-spin conversion. This explains the non-zero η^y_{zz}. A similar consideration explains the non-zero η^z_{yz} as well.

To qualitatively explain the key experimental observation (Fig. 4b), we calculate the d dependence of the y- and z-spin accumulations at the surface of the WTe_2 side in the $PtTe_2$ (d)/WTe_2 (8 − d) bilayers using the spin drift-diffusion formalism[33,34], including the spin-to-spin conversion contribution (Supplementary Note 11 for details of the drift-diffusion model and calculation). Figure 4d shows the computed d dependence of the y- and z-spin accumulations, which is in qualitative agreement with the experimental result of Fig. 4b, suggesting that the spin-to-spin conversion by the crystal asymmetry of WTe_2 is responsible for the large increase in $\sigma_{s,z}$ for the bilayer. We also carry out first-principles calculations for three different $PtTe_2$ (6 − n)/WTe_2 (n) structures for n = 0, 3 and 6, where n is the number of van der Waals layers, and the results are consistent with the spin-to-spin conversion by the crystal asymmetry of WTe_2 (Supplementary Note 12). Therefore, our theoretical and numerical results collectively establish that the spin-to-spin conversion by the crystal asymmetry of WTe_2 is present in the $PtTe_2/WTe_2$ bilayer and is the dominant contributor to our experimental observations.

Now, we explain our experimental results based on the spin-to-spin conversion mechanism. The spin-torque efficiency and field-free switching of the perpendicular magnetization are determined by the y and z spins. While y spins are generated through charge-to-spin conversion in both the $PtTe_2$ and WTe_2 layers, the z spins are mostly a result of charge-to-spin and spin-to-spin conversions solely within the WTe_2 layer. The introduction of $PtTe_2$ diverts a substantial portion of the current (over 68 percent) through the $PtTe_2$ layer (Supplementary Table 3), leading to a weakened charge-to-spin conversion within the WTe_2, manifested as a decrease in θ_y and θ_z with increasing d (Fig. 4a). The higher current flowing through $PtTe_2$, combined with its high spin Hall conductivity, generates significant y spins within the $PtTe_2$ layer,

a considerable proportion of which are subsequently injected into the WTe_2 layer. These injected *y* spins turn into *z*-polarized spins due to the spin-to-spin conversion within the symmetry-broken WTe_2 layer, thereby contributing to the observed increase in $\sigma_{s,z}$ (Fig. 4b). Since the *z* spins generated by charge-to-spin conversion in WTe_2 are minimal, the conversion from *z* to *y* spins within the $PtTe_2$ layer is negligible. Consequently, in samples with $d = 0.5$ and 2.0, a full, field-free switching of perpendicular magnetization can be achieved (Fig. 3), due to an ample supply of *z* spins.

However, for samples with $d > 3.5$ nm, the WTe_2 is too thin compared to its spin precession length, which is the relevant length scale for spin-to-spin conversion due to the lateral symmetry breaking of WTe_2 (Supplementary Note 11). As a result, for thin WTe_2, the injected *y* spins from the $PtTe_2$ layer do not convert efficiently to *z* spins but instead tend to maintain their original orientation, leading to a decrease in $\sigma_{s,z}$ approaching zero. Consequently, field-free switching cannot be achieved in samples with $d = 5.0$ and 6.5 nm due to insufficient *z* spins. Meanwhile, a field-assisted switching can be observed with the assistance of a 10 mT magnetic field (Supplementary Fig. 37).

Finally, we discuss the merits of the heterostructure design introduced in this work. The combination of the generation of *z* spins and high spin Hall conductivity, which is desirable for SOT applications, is hard to achieve in a single material system. These challenges are due to the low spin Hall conductivity of typical low-symmetry materials, and the trade-off between the electrical conductivity and effective spin Hall angle[35,36]. For example, as summarized in Supplementary Table 1, various WTe_2 samples fabricated by different methods, such as mechanical exfoliation[11,13], chemical vapour deposition[14] and MBE, exhibit a similar value of the spin Hall conductivity, $\sigma_{s,y} \approx 1 \times 10^4 \times \hbar/2e\ \Omega^{-1}\,m^{-1}$, even though their electrical conductivities are different. The above limitation can be mitigated by heterostructure engineering. The $\sigma_{s,y}$ value ($\approx 2.35 \times 10^5 \times \hbar/2e\ \Omega^{-1}\,m^{-1}$) of the $PtTe_2/WTe_2$ bilayers is higher than many two-dimensional van der Waals materials[7,11–14,27,37,38] and is even comparable to that of topological insulators[17,18] and HMs[19,20]. More importantly, the spin-to-spin conversion in symmetry-broken WTe_2 leads to the highest value of $\sigma_{s,z}$ ($\approx 0.25 \times 10^5 \times \hbar/2e\ \Omega^{-1}\,m^{-1}$) in the $PtTe_2/WTe_2$ bilayers, surpassing that of other low-symmetry materials[7,11,14] and antiferromagnets[39,40] (Fig. 4e). Note that it is not possible to maintain the required symmetry of WTe_2 on top of a conventional HM, such as Pt; therefore, the combination of the $PtTe_2/WTe_2$ bilayer is unique. The high $\sigma_{s,z}$ value guarantees an all-electric manipulation of the perpendicular magnetization at low power consumption without any external magnetic field. The significance of the *z*-spin generation is further exemplified by the symmetry-dependent SOT measurements performed on the $PtTe_2$ (2 nm)/WTe_2 (6 nm)/CoFeB sample (Supplementary Note 13). The realization of two-dimensional heterostructures with both high spin Hall conductivity and *z* spins significantly enhances the SOT performance, and thus, we anticipate SOT heterostructure engineering may expand to other materials systems.

Online content

Any methods, additional references, Nature Portfolio reporting summaries, source data, extended data, supplementary information, acknowledgements, peer review information; details of author contributions and competing interests; and statements of data and code availability are available at https://doi.org/10.1038/s41563-023-01774-z.

References

1. Liu, L., Lee, O. J., Gudmundsen, T. J., Ralph, D. C. & Buhrman, R. A. Current-induced switching of perpendicularly magnetized magnetic layers using spin torque from the spin Hall effect. *Phys. Rev. Lett.* **109**, 096602 (2012).
2. Emori, S., Bauer, U., Ahn, S. M., Martinez, E. & Beach, G. S. Current-driven dynamics of chiral ferromagnetic domain walls. *Nat. Mater.* **12**, 611–616 (2013).
3. Haazen, P. P. et al. Domain wall depinning governed by the spin Hall effect. *Nat. Mater.* **12**, 299–303 (2013).
4. Miron, I. M. et al. Perpendicular switching of a single ferromagnetic layer induced by in-plane current injection. *Nature* **476**, 189–193 (2011).
5. Baek, S. C. et al. Spin currents and spin–orbit torques in ferromagnetic trilayers. *Nat. Mater.* **17**, 509–513 (2018).
6. Liu, Y. & Shao, Q. Two-dimensional materials for energy-efficient spin–orbit torque devices. *ACS Nano* **14**, 9389–9407 (2020).
7. Stiehl, G. M. et al. Layer-dependent spin-orbit torques generated by the centrosymmetric transition metal dichalcogenide β–$MoTe_2$. *Phys. Rev. B* **100**, 184402 (2019).
8. Song, P. et al. Coexistence of large conventional and planar spin Hall effect with long spin diffusion length in a low-symmetry semimetal at room temperature. *Nat. Mater.* **19**, 292–298 (2020).
9. Liu, L. et al. Symmetry-dependent field-free switching of perpendicular magnetization. *Nat. Nanotechnol.* **16**, 277–282 (2021).
10. Stiehl, G. M. et al. Current-induced torques with Dresselhaus symmetry due to resistance anisotropy in 2D materials. *ACS Nano* **13**, 2599–2605 (2019).
11. MacNeill, D. et al. Control of spin–orbit torques through crystal symmetry in WTe_2/ferromagnet bilayers. *Nat. Phys.* **13**, 300–305 (2017).
12. MacNeill, D. et al. Thickness dependence of spin-orbit torques generated by WTe_2. *Phys. Rev. B* **96**, 054450 (2017).
13. Shi, S. et al. All-electric magnetization switching and Dzyaloshinskii–Moriya interaction in WTe_2/ferromagnet heterostructures. *Nat. Nanotechnol.* **14**, 945–949 (2019).
14. Shi, S. et al. Observation of the out-of-plane polarized spin current from CVD grown WTe_2. *Adv. Quantum Technol.* **4**, 2100038 (2021).
15. Xie, Q. et al. Field-free magnetization switching induced by the unconventional spin–orbit torque from WTe_2. *APL Mater.* **9**, 051114 (2021).
16. Kao, I. H. et al. Deterministic switching of a perpendicularly polarized magnet using unconventional spin–orbit torques in WTe_2. *Nat. Mater.* **21**, 1029–1034 (2022).
17. Mellnik, A. R. et al. Spin-transfer torque generated by a topological insulator. *Nature* **511**, 449–451 (2014).
18. DC, M. et al. Room-temperature high spin–orbit torque due to quantum confinement in sputtered $Bi_xSe_{(1-x)}$ films. *Nat. Mater.* **17**, 800–807 (2018).
19. Liu, L., Moriyama, T., Ralph, D. C. & Buhrman, R. A. Spin-torque ferromagnetic resonance induced by the spin Hall effect. *Phys. Rev. Lett.* **106**, 036601 (2011).
20. Liu, L. et al. Spin-torque switching with the giant spin Hall effect of tantalum. *Science* **336**, 555–558 (2012).
21. Geim, A. K. & Grigorieva, I. V. Van der Waals heterostructures. *Nature* **499**, 419–425 (2013).
22. Novoselov, K. S., Mishchenko, A., Carvalho, A. & Castro Neto, A. H. 2D materials and van der Waals heterostructures. *Science* **353**, aac9439 (2016).
23. Sierra, J. F., Fabian, J., Kawakami, R. K., Roche, S. & Valenzuela, S. O. Van der Waals heterostructures for spintronics and opto-spintronics. *Nat. Nanotechnol.* **16**, 856–868 (2021).
24. Yang, H. et al. Two-dimensional materials prospects for non-volatile spintronic memories. *Nature* **606**, 663–673 (2022).
25. Fang, D. et al. Spin–orbit-driven ferromagnetic resonance. *Nat. Nanotechnol.* **6**, 413–417 (2011).
26. Chen, X. et al. Observation of the antiferromagnetic spin Hall effect. *Nat. Mater.* **20**, 800–804 (2021).
27. Xu, H. et al. High spin Hall conductivity in large-area type-II Dirac semimetal $PtTe_2$. *Adv. Mater.* **32**, e2000513 (2020).

28. Zhu, L. et al. Strong damping-like spin-orbit torque and tunable Dzyaloshinskii–Moriya interaction generated by low-resistivity $Pd_{1-x}Pt_x$ alloys. *Adv. Funct. Mater.* **29**, 1805822 (2019).
29. Lifshits, M. B. & Dyakonov, M. I. Swapping spin currents: interchanging spin and flow directions. *Phys. Rev. Lett.* **103**, 186601 (2009).
30. Saidaoui, H. B. & Manchon, A. Spin-swapping transport and torques in ultrathin magnetic bilayers. *Phys. Rev. Lett.* **117**, 036601 (2016).
31. Park, H. J. et al. Spin swapping effect of band structure origin in centrosymmetric ferromagnets. *Phys. Rev. Lett.* **129**, 037202 (2022).
32. Lin, W. et al. Evidence for spin swapping in an antiferromagnet. *Nat. Phys.* **18**, 800–805 (2022).
33. Valet, T. & Fert, A. Theory of the perpendicular magnetoresistance in magnetic multilayers. *Phys. Rev. B* **48**, 7099–7113 (1993).
34. Haney, P. M., Lee, H.-W., Lee, K.-J., Manchon, A. & Stiles, M. D. Current induced torques and interfacial spin-orbit coupling: semiclassical modeling. *Phys. Rev. B* **87**, 174411 (2013).
35. Wang, Y., Deorani, P., Qiu, X., Kwon, J. H. & Yang, H. Determination of intrinsic spin Hall angle in Pt. *Appl. Phys. Lett.* **105**, 152412 (2014).
36. Shao, Q. et al. Roadmap of spin–orbit torques. *IEEE Trans. Magn.* **57**, 800439 (2021).
37. Guimaraes, M. H. D., Stiehl, G. M., MacNeill, D., Reynolds, N. D. & Ralph, D. C. Spin–orbit torques in $NbSe_2$/permalloy bilayers. *Nano Lett.* **18**, 1311–1316 (2018).
38. Liang, S. et al. Spin-orbit torque magnetization switching in $MoTe_2$/permalloy heterostructures. *Adv. Mater.* **32**, e2002799 (2020).
39. Nan, T. et al. Controlling spin current polarization through non-collinear antiferromagnetism. *Nat. Commun.* **11**, 4671 (2020).
40. Bose, A. et al. Tilted spin current generated by the collinear antiferromagnet ruthenium dioxide. *Nat. Electron.* **5**, 267–274 (2022).

Methods

MBE growth of $PtTe_2$/WTe_2 heterostructures

WTe_2, $PtTe_2$ and $PtTe_2$/WTe_2 films were grown on sapphire Al_2O_3(001) substrates using a MBE system with a base pressure of 1×10^{-9} mbar. The Al_2O_3 substrates were first soaked in deionized water at 90 °C for 2 h and thermally annealed at 1,000 °C for 3 h in a tube furnace with flowing oxygen gas. The heat-treated Al_2O_3 substrates were then degassed at ~800 °C for 1 h in the MBE chamber. High-purity W (4N) and Pt (4N) were evaporated from electron-beam evaporators, and Te (5N) was evaporated from a Knudsen cell. During the growth of the films, the substrate was maintained at ~250 °C. The growth process was monitored by reflection high-energy electron diffraction. The flux ratio of Te/(Pt or W) was set to be >30 to avoid a possible Te deficiency in the samples. The growth rate of the $PtTe_2$ and WTe_2 was around 0.05 nm min^{-1}. When the growth was finished, the samples were slowly cooled to room temperature.

Magnetron sputtering growth of ferromagnetic layers

The MBE-grown films were immediately transferred into a magnetron sputtering chamber in the standard clean room environment with a well-controlled level of constant temperature and low humidity. The transfer time was strictly controlled to be under 3 min before pumping down the sputtering chamber. The perpendicularly magnetized ferromagnetic layer Ti (2)/$Co_{0.2}Fe_{0.6}B_{0.2}$ (0.9)/MgO (2)/Ta (1.5) (numbers in parentheses are in nanometres) was subsequently sputtered on the top of the MBE films at room temperature. For the ST-FMR devices, the ferromagnetic layer of $Ni_{81}Fe_{19}$ (6)/SiO_2 (2)/Ta (1.5) (numbers in parentheses are in nanometres) with in-plane magnetic anisotropy was grown on the top of the MBE films at room temperature.

Device fabrication

The films were patterned into a 40 μm × 20 μm Hall bar by optical lithography and Ar ion milling. Ta (5 nm)/Cu (120 nm)/Ta (5 nm) electrodes were deposited by magnetron sputtering.

Current-induced switching measurements

A Keithley 6221 was used as the current source for d.c. and pulse measurements. For the pulse measurements, a 100 μs pulse was first applied, and then a small d.c. current of 50 μA was applied to measure the Hall resistance. The Hall voltage was measured using a Keithley 2182A nanovoltmeter.

Data availability

The data that support the findings of this study are available from H.Y. (experiment) or K.-J.L. (theory) upon reasonable request.

Code availability

The codes that calculate non-equilibrium spin densities can be accessed from K.-J.L. upon reasonable request.

Acknowledgements

This research was supported by the SpOT-LITE programme (A*STAR grant, A18A6b0057) through RIE2020 funds (H.Y.); the National Research Foundation (NRF) Singapore Investigatorship (NRFI06-2020-0015; H.Y.); Samsung Electronics' University R&D programme, Samsung Electronics (IO221024-03172-01; H.Y.); the National Research Foundation of Korea (NRF-2020R1A2C3013302; K.-J.L.); the Nano & Material Technology Development Program through the National Research Foundation of Korea funded by the Ministry of Science and ICT (2022M3H4A1A04098811; K.-J.L.); and the KIST institutional programmes (2E32251 and 2E32252; K.-W.K.).

Author contributions

F.W. and H.Y. conceived and designed the experiments. F.W., G.S. and S.Y. grew the samples. F.W. carried out the reflection high-energy electron diffraction, atomic force microscopy, transport and switching measurements and analysed the data. G.S. performed the ST-FMR measurements. D.Y. performed the Raman and terahertz measurements. K.L. carried out the X-ray diffraction measurements. G.S., Y.L. and S.Z. performed the device fabrications. H.R.T. and M.L. carried out the transmission electron microscopy measurements under the supervision of A.S.; K.-W.K. developed the analytic theories, and H.-J.P. and J.G.J. performed the first-principles calculations under the supervision of K.-J.L.; and T.K. performed the macro-spin simulations. F.W., H.Y., K.-W.K. and K.-J.L. wrote the manuscript with contributions from all authors. H.Y. supervised the experimental aspects, and K.-J.L. supervised the theoretical aspects. All authors discussed the results and commented on the manuscript.

Competing interests

The authors declare no competing interests.

Additional information

Supplementary information The online version contains supplementary material available at https://doi.org/10.1038/s41563-023-01774-z.

Correspondence and requests for materials should be addressed to Kyung-Jin Lee or Hyunsoo Yang.

Peer review information *Nature Materials* thanks the anonymous reviewers for their contribution to the peer review of this work.